

## Full length article

# Design and synthesis of a magnesium alloy for room temperature hydrogen storage

Kaveh Edalati<sup>a, b, \*</sup>, Ryoko Uehiro<sup>b</sup>, Yuji Ikeda<sup>c</sup>, Hai-Wen Li<sup>a, d, \*\*</sup>, Hoda Emami<sup>a</sup>, Yaroslav Filinchuk<sup>e</sup>, Makoto Arita<sup>b</sup>, Xavier Sauvage<sup>f</sup>, Isao Tanaka<sup>c, g</sup>, Etsuo Akiba<sup>a, d, h</sup>, Zenji Horita<sup>a, b</sup>

<sup>a</sup> WPI, International Institute for Carbon-Neutral Energy Research (WPI-I2CNER), Kyushu University, Fukuoka 819-0395, Japan

<sup>b</sup> Department of Materials Science and Engineering, Faculty of Engineering, Kyushu University, Fukuoka 819-0395, Japan

<sup>c</sup> Center for Elements Strategy Initiative for Structure Materials (ESISM), Kyoto University, Sakyo, Kyoto 606-8501, Japan

<sup>d</sup> International Research Center for Hydrogen Energy, Kyushu University, Fukuoka 819-0395, Japan

<sup>e</sup> Université Catholique de Louvain, 1348 Louvain-la-Neuve, Belgium

<sup>f</sup> Normandie Université, UNIROUEN, INSA Rouen, CNRS, Groupe de Physique des Matériaux, 76000 Rouen, France

<sup>g</sup> Department of Materials Science and Engineering, Kyoto University, Kyoto 606-8501, Japan

<sup>h</sup> Department of Mechanical Engineering, Faculty of Engineering, Kyushu University, Fukuoka 819-0395, Japan



## ARTICLE INFO

## Article history:

Received 5 October 2017

Accepted 13 February 2018

Available online 21 February 2018

## Keywords:

Metal hydrides

Hydrogen storage

First-principles calculations

Mechanical alloying

Severe plastic deformation (SPD)

## ABSTRACT

Safe and high-density storage of hydrogen is a key issue for development of hydrogen as a clean energy carrier. Hydride-forming materials are potential candidates for safe and high-density storage of hydrogen and among them; Mg-based alloys are the most investigated ones due to their high gravimetric capacity. The key issue for practical application of Mg-based alloys is that they do not desorb hydrogen without heating due to the strong hydrogen binding energy. In this study, we employed first-principles calculations to design a Mg-based alloy with a low hydrogen binding energy and room temperature hydrogen storage properties. The designated material, highly-homogenous Mg<sub>4</sub>NiPd with a BCC-based CsCl-type structure, was successfully synthesized by severe plastic deformation via the high-pressure torsion (HPT) method. The alloy exhibited reversible hydrogenation and dehydrogenation at room temperature with high phase stability. This discovery introduces a rational approach to design and synthesize new alloys for hydrogen storage using the concept of binding energy engineering.

© 2018 Acta Materialia Inc. Published by Elsevier Ltd. All rights reserved.

## 1. Introduction

Hydrogen is currently considered to be an important future energy carrier [1]. Despite significant interest in hydrogen as a clean fuel with zero CO<sub>2</sub> emissions, there are still considerable issues that need to be addressed for the future application of hydrogen as a fuel. Among these issues, the design of new technology to store hydrogen safely, with high volumetric and gravimetric density and without using a heating system is a major challenging task [1]. Since hydrogen is the lightest known element,

its storage in the form of gas under ambient pressure is impractical and requires a very large volume per kilogram. Hydrogen storage in the form of compressed gas, usually at several hundred bars, is being commercialized for automobiles, but compressed hydrogen gas requires special and expensive tanks to ensure hydrogen is stored safely [1]. Hydrogen storage in the form of liquid is being used in aerospace industry, but large energy levels are required for liquefaction and the hydrogen loss through evaporation is another issue [1].

One promising technique for the high-density and safe storage of hydrogen is the use of different hydrides such as Mg-based, Ti-based, La-based or complex hydrides [2,3]. Mg-based hydrides, which are known as the first introduced hydrogen storage candidate materials [4], are the most investigated metal hydrides due to their large volumetric and gravimetric storage capacity [2]. Despite high-density storage capacity of Mg-based hydrides, their main drawback is still their high thermodynamic stability due to the

\* Corresponding author. WPI, International Institute for Carbon-Neutral Energy Research (WPI-I2CNER), Kyushu University, Fukuoka 819-0395, Japan.

\*\* Corresponding author. WPI, International Institute for Carbon-Neutral Energy Research (WPI-I2CNER), Kyushu University, Fukuoka 819-0395, Japan.

E-mail addresses: [kaveh.edalati@zaiko6.zaiko.kyushu-u.ac.jp](mailto:kaveh.edalati@zaiko6.zaiko.kyushu-u.ac.jp) (K. Edalati), [li.haiwen.305@m.kyushu-u.ac.jp](mailto:li.haiwen.305@m.kyushu-u.ac.jp) (H.-W. Li).

strong metal-hydrogen binding energy and thus their high dehydrogenation temperature (maximum ~630 K for pure MgH<sub>2</sub> and minimum ~460 K for Mg<sub>2</sub>NiH<sub>4</sub>, while the desirable temperatures are below 373 K and ideally room temperatures) [2]. Despite this apparent thermodynamic barrier to reduce the dehydrogenation temperature of Mg-based materials to room temperature [5], it was shown that the Mg-H binding can be broken at room temperature in a few compounds based on rare-earth elements and/or Ca with the Mg addition [6–9]. Refs. [6–9] suggest that room temperature hydrogen storage is still achievable in Mg-based alloys, provided that the alloys with low hydrogen binding energy can be designed and synthesized successfully.

The main strategy currently used to reduce the dehydrogenation temperature of hydrogen storage materials is to mix elements with two different hydrogen affinities, specifically: an element that readily reacts with hydrogen, such as Mg, Ti or La (component A) with negative binding energies, and an element that has no affinity to react with hydrogen, such as Ni or Fe (component B) with positive binding energies [1]. This strategy has been successfully employed to fabricate binary Ti-based (AB-type TiFe) [10] and La-based (AB<sub>5</sub>-type LaNi<sub>5</sub>) compounds [11] that can reversibly store hydrogen at room temperature. In the case of the Mg-based binary systems, however, they can only function above ~460 K, with A<sub>2</sub>B-type Mg<sub>2</sub>Ni exhibiting the lowest temperature [4,5].

In a previous study, we calculated the hydrogen binding energy in different binary Mg-based systems from first-principles and compared the results with experimentally measured dehydrogenation temperatures [12]. We found that intermetallic materials, such as Mg<sub>2</sub>Ni and Mg<sub>2</sub>Co with dehydrogenation temperatures lower than pure Mg, reduce the hydrogen binding energy to less negative values. However, some other intermetallics, such as Mg<sub>2</sub>Pd, Mg<sub>2</sub>Sn, Mg<sub>2</sub>Si, Mg<sub>2</sub>Ge, Mg<sub>2</sub>In and MgAg have positive hydrogen binding energies and thus cannot absorb hydrogen. The target hydrogen binding energy for room-temperature hydrogen storage is a negative value close to zero, but none of the current Mg-based binary systems meet this target.

As briefly summarized in Fig. 1(a), to engineer new three-component (ternary) Mg-based compounds with a low hydrogen binding energy close to zero, our strategy is mixing two different types of binary compounds at the atomic scale: (A') a compound with a negative hydrogen binding energy (such as Mg<sub>2</sub>Ni) and (B') a compound with a positive hydrogen binding energy (such as Mg<sub>2</sub>Pd). Although many different composition can be fabricated by mixing the compounds with negative and positive hydrogen binding energies, we selected Mg<sub>4</sub>NiPd (Mg<sub>2</sub>Ni + Mg<sub>2</sub>Pd) among many other possible choices because of well-know catalytic effect of Ni and Pd elements on hydrogen storage in Mg-based alloys [2], which minimizes the effect of kinetic issues on the experimental results.

Although the above-mentioned strategy seems feasible from a theoretical perspective, there are some technical limitations to mixing these compounds homogeneously and achieve a uniform atomic-scale elemental distribution (i.e. a homogenous single phase) because of the thermodynamic immiscibility of Mg in many different systems [13]. For example, if Mg<sub>4</sub>NiPd is fabricated by slow solidification, three phases (Mg, Mg<sub>2</sub>Ni and Mg<sub>6</sub>Pd) with heterogeneous elemental distributions are formed, as reported in the ternary phase diagram of Mg-Ni-Pd [14,15]. One effective solution for atomic-scale mixing of Mg with other elements at the atomic scale is the application of severe plastic deformation (SPD) using high-pressure torsion (HPT) (see the following references for more information on the principles of SPD [16,17] and the details and background of HPT [18,19]). As a brief description, in the HPT method as schematically shown in Fig. 1(b), a disc sample is compressed between two anvils under high pressure and concurrently

subjected to severe strain by rotating one of the anvils with respect to the other anvil for *N* turns. Earlier studies showed that the HPT method is quite effective for synthesizing new Mg-based compounds [20,21], even in immiscible systems. HPT has also been used to activate hydrogen storage materials [22,23] and to enhance the hydrogenation kinetics in pure Mg [24,25], Mg-based composites [26,27], and Mg alloys [28,29].

The goal of this study is to propose a strategy of designing and synthesizing new compounds with promising functionality, i.e. a new Mg-based alloy that can reversibly store hydrogen at room temperature. Here, we report the successful design and fabrication of a Mg<sub>4</sub>NiPd alloy with the BCC-based CsCl-type structure, which is thermally stable up to 440 K and reversibly store 0.7 wt% of hydrogen at room temperature. Despite low hydrogen storage capacity of the alloy, this study opens up a rational approach to design and synthesize new materials beyond the scope of known equilibrium phase diagrams for promising functions such as room temperature hydrogen storage.

## 2. Materials and methods

### 2.1. Materials processing

Small pieces of high-purity (>99%) Mg, Ni and Pd with a nominal composition of Mg<sub>4</sub>NiPd were melted under an argon atmosphere and cast into a metallic mold to fabricate a rod with a 12-mm diameter and a 16-mm length. The as-cast material was subjected to SPD using the HPT process [16–19] to achieve a single phase with an atomic-scale elemental distribution. To do this, the rod was first sliced into discs 0.8 mm thick and 10 mm diameter, with each disc being further processed by HPT under a pressure of *P* = 6 GPa at room temperature for either *N* = 20, 100, 500 or 1500 turns with a rotation speed of  $\omega = 1$  rpm.

### 2.2. Materials characterization

Following the HPT processing, the discs were polished by mechanical grinding and buffing to mirror-like surfaces, and the elemental distribution was examined at the mid-radius of the discs by a scanning electron microscope (SEM) equipped with an energy dispersive X-ray spectroscopy (EDS) using an accelerating voltage of 15 kV.

The elemental mixing and the formation of new phases were studied using X-ray diffraction (XRD) analysis with Cu K $\alpha$  radiation produced using a current of 40 mA and an accelerating voltage of 40 kV. The XRD patterns were examined in detail using the Rietveld method in the FullProf Suite software [30,31].

To examine the final microstructure of the alloys after 1500 HPT turns, a thin foil was prepared 4 mm away from the disc center using a focused ion beam (FIB) system. It should be noted that after such large numbers of HPT turns, microstructure and properties do not vary radially in the samples [32–34]. The foil was examined with transmission electron microscopy (TEM) in bright-field (BF), dark-field (DF), selected-area electron diffraction (SAED) and high-resolution modes using an accelerating voltage of 200 or 300 kV.

The spatial distribution of the three elements was then characterized after 1500 HPT turns at the atomic scale using atom probe tomography (APT). Samples were prepared using a FIB system using the lift-out method at a distance of 4 mm from the disc center. APT analysis was carried out using a LEAP 4000HR instrument at a temperature of 40 K with electric pulses with a 20% pulse fraction, and a 200 kHz pulse repetition rate. Three dimensional reconstructions were generated using the Integrated Visualization & Analysis Software (IVAS) and other data processing was performed with the GPM 3D-soft (Groupe de Physique des Matériaux 3D-soft).

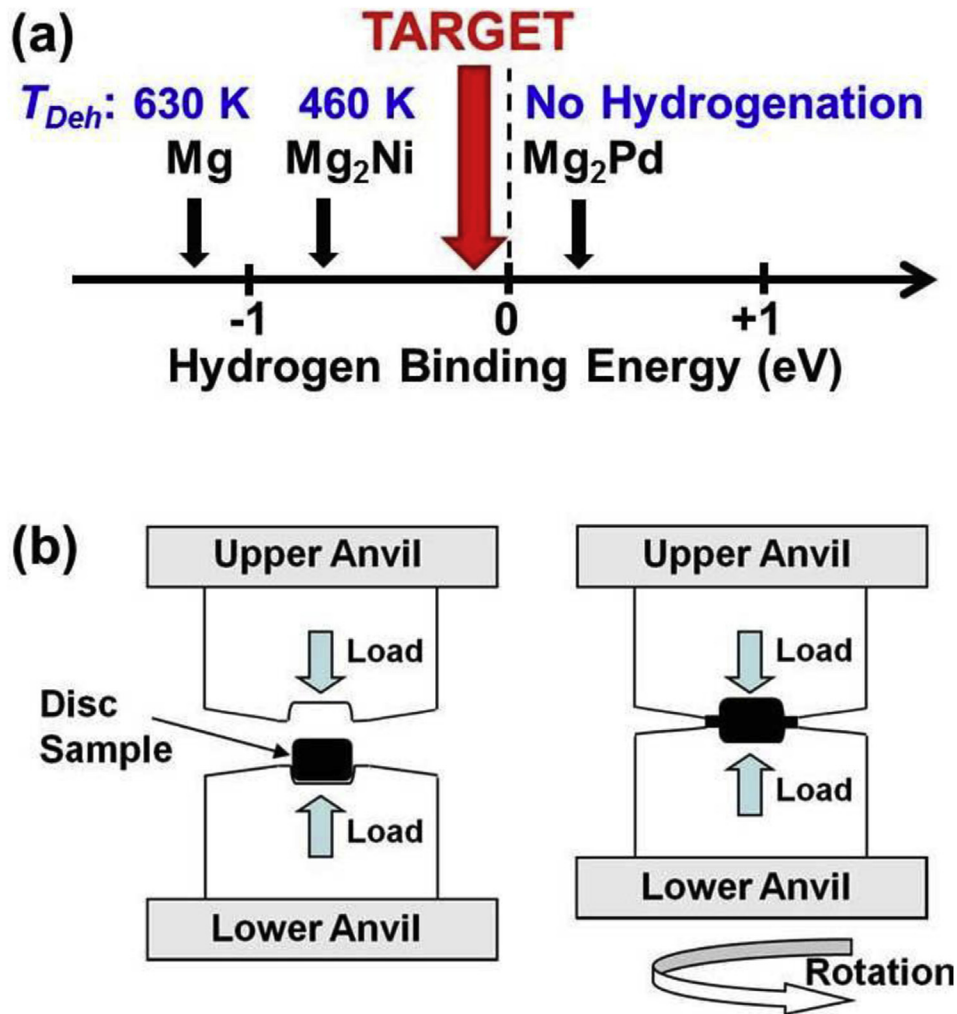


**Fig. 1.** (a) Schematic illustration of the hydrogen binding energy effects on the hydrogen storage behavior of materials in the Mg-Ni-Pd system; and (b) schematic illustration of high-pressure torsion (HPT) method. Data for the hydrogen binding energy and dehydrogenation temperatures ( $T_{DeH}$ ) in (a) were taken from Emami et al. [12].

### 2.3. Hydrogen storage

The hydrogen storage performance of the samples was examined in a Sieverts-type gas absorption apparatus. One disc sample processed using HPT for 1500 turns was broken to pieces with dimensions smaller than 0.1 mm under an argon atmosphere and subjected to evacuation at room temperature for 2 h to remove possible moistures. The pressure-composition isotherm (PCI) measurements were performed at 305 K up to a hydrogen pressure of 10 MPa for several hydrogenation/dehydrogenation cycles. After the PCI measurements were taken, each sample was examined by XRD analysis.

Finally, hydrogenation behavior of the HPT-synthesized phase and its thermal stability were examined by *in situ* XRD analysis using synchrotron radiation with a wavelength of 0.07149 nm either under an argon atmosphere during heating, or at room temperature under a hydrogen atmosphere at a pressure of 1.1 MPa (the maximum achievable hydrogen pressure in the facility) at SNBL, ERSF, Grenoble, France.

### 2.4. Calculation methods

The crystal structure of the  $Mg_4NiPd$  and its hydrogen binding energy were examined theoretically from first-principles. Since a

BCC-based crystal structure was experimentally detected in different Mg-based alloys such as Mg-Ni [35],  $Mg_{50}Ni_{45}Pd_5$  [36], Mg-Ni-V [20], Mg-Pd-V [20], Mg-Ti [37], Mg-Zr [21] and Mg-V [20] after SPD processing by ball milling [35,36] or HPT [20,21,37], the initial structure was modeled by a 54-atom supercell constructed from  $3 \times 3 \times 3$  BCC unit cells. A random configuration of the constituent elements was simulated using a special quasi-random structure (SQS) [38–40], in which the center sites were occupied by Mg atoms and the corner sites were randomly occupied by either Mg, Ni or Pd (CsCl-type based on our preliminary experimental data). The SQS was obtained by application of the CLUPAN code [41,42]. The calculations were conducted with the plane-wave basis projector augmented wave (PAW) method [43] in the framework of density functional theory (DFT) within the generalized gradient approximation (GGA) of the Perdew-Burke-Ernzerhof (PBE) form [44], as implemented in the VASP (Vienna Ab initio Simulation Package) code [45–47]. A plane-wave energy cutoff of 350 eV was used. The Brillouin zone was sampled with a  $\Gamma$ -centered  $15 \times 15 \times 15$  k-point mesh per BCC unit cell using the Methfessel-Paxton scheme [48] with a smearing width of 0.4 eV. The crystal structure was optimized until the energy convergences and the residual forces decreased to less than  $10^{-8}$  eV and  $1 \times 10^{-3}$  eV/Å, respectively. The optimized crystal structure was visualized three dimensionally by employing the VESTA code [49].

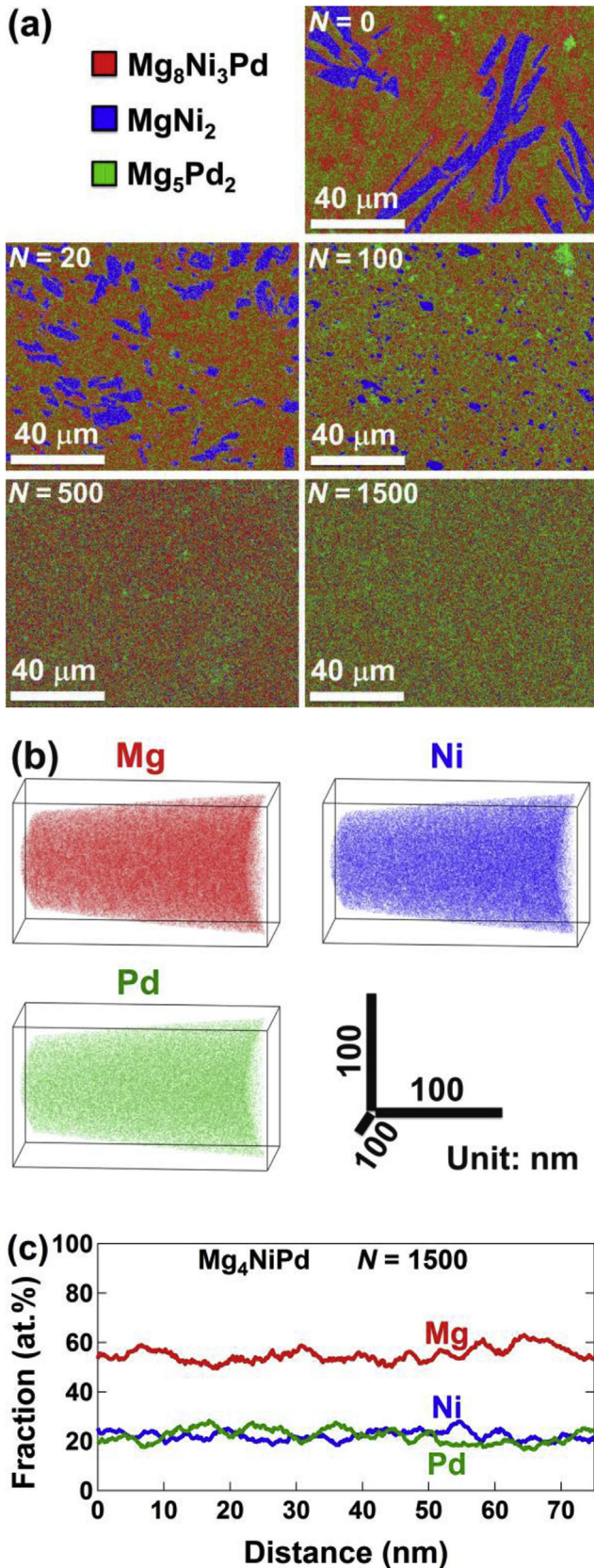


**Fig. 2.** The distribution of Mg, Ni and Pd in the alloy becomes more homogeneous with increased HPT turns and a uniform atomic-scale elemental distribution is achieved after 1500 turns. (a) SEM-EDS elemental mapping of the  $Mg_4NiPd$  processed for 0–1500 turns. (b) APT elemental mapping and (c) typical composition profile (atomic

Phonon calculations were performed using the PHONOPY code [50] in order to examine the dynamic stability of the optimized crystal structure. Force constants were obtained for the 54-atom supercell model using an atomic displacement of 1 p.m. Phonon frequencies at reciprocal-space points were calculated using  $\Gamma$ -centered  $64 \times 64 \times 64$  meshes, and the phonon density of states was calculated using the tetrahedron method [51,52].

Hydrogen binding energies were calculated for the three primary types of octahedral sites, namely,  $4Mg-2Ni$ ,  $4Mg-1Ni-1Pd$  and  $4Mg-2Pd$ , since these could be found the most frequently in the supercell model. Hydrogen atoms were located in the selected sites and the structures were optimized in terms of their lattice shape and atomic positions. The theoretical hydrogen binding energies were calculated using the following equation, as described previously [12]:

$$\Delta E = E(Mg_4NiPdH) - \left[ E(Mg_4NiPd) + \frac{1}{2}E(H_2) \right] \quad (1)$$

In this equation,  $\Delta E$  is the hydrogen binding energy and  $E$  denotes the internal energies at 0 K.

### 3. Results and discussion

#### 3.1. Experimental evidence for atomic-scale mixing and new phase formation

In order to manipulate the hydrogen binding energy, it is essential to generate an atomic-scale uniform distribution of elements and form a single phase. To do this, the as-cast material was processed by HPT for 20, 100, 500 and 1500 turns and the distribution of elements was examined by SEM-EDS, STEM and APT. Moreover, the formation of new single phase and its structure were examined by XRD and TEM.

To assess the distribution of the elements in the alloy, we analyzed the mid-radius of the discs by SEM-EDS. Fig. 2(a) shows the SEM-EDS analysis of samples. The as-cast sample ( $N = 0$ ) contained three intermetallic phases with the compositions  $Mg_8Ni_3Pd$ ,  $MgNi_2$  and  $Mg_5Pd_2$ , as measured by EDS analysis quantitatively. The formation of these three intermetallics is not consistent with the reported ternary phase diagrams of Mg–Ni–Pd, in which the  $Mg_4NiPd$  composition should contain Mg,  $Mg_2Ni$  and  $Mg_6Pd$  [14,15]. The reason for this contradiction is that the ingot was casted in a metallic mold which resulted in rapid cooling rate and formation of three metastable phases. The three intermetallic phases are well distinguished after the HPT processing for 20 and 100 turns, but their sizes become considerably smaller, as reported for many other HPT-processed multi-phase systems [20,32]. The three phases can barely be distinguished after 500, and after 1500 turns, the elemental distribution becomes homogeneous within the detection limits of SEM-EDS.

Since the SEM-EDS method with low detection limit can not show the atomic-scale homogeneity, the distribution of the three elements at the atomic scale was examined by APT analyses. The APT mappings in Fig. 2(b) show that the distribution of the three elements at the atomic level occurred after 1500 turns. The uniform atomic-scale distribution of the three elements is more apparent in the line profiles of Fig. 2(c) which show that the compositional fluctuations are  $\pm 7$  at.% for Mg and  $\pm 4$  at.% for Ni and Pd.

fraction of Mg, Ni and Pd versus location) for the  $Mg_4NiPd$  processed for 1500 turns. The vertical axis in (a) signifies the shearing direction during HPT processing; the dimensions of cuboids in (b) are  $111 \times 111 \times 200 \text{ nm}^3$ .

Importantly, two other volumes analyzed by APT exhibited similar features with reasonable atomic-scale elemental homogeneity (see the supporting video), which is essential to tune the atomic sites for a low hydrogen binding energy [12].

Supplementary video related to this article can be found at <https://doi.org/10.1016/j.actamat.2018.02.033>.

To assess the formation of a new single phase, we analyzed the materials by XRD analyses. The XRD profiles in Fig. 3(a) shows that the peaks for the three initial intermetallics ( $\text{Mg}_8\text{Ni}_3\text{Pd}$ ,  $\text{MgNi}_2$  and  $\text{Mg}_5\text{Pd}_2$ ) are clearly visible for the ingot ( $N=0$ ), which is in good agreement with the SEM-EDS analysis shown in Fig. 2(a). After 20 and 100 turns, the intermetallic peaks for the three species are still visible, but with considerable peak-broadening. Such peak broadenings confirm that large number of lattice defects, including dislocations [33] and grain boundaries [34], is formed after the HPT processing. It was suggested previously that the formation of these lattice defects is one main mechanism for the atomic-scale elemental distribution and formation of new phases after SPD processing [53–55]. The peak intensity for the three intermetallics greatly decreases after 500 turns, and a new single phase with a BCC-based partly ordered CsCl-type structure and a lattice parameter of  $a=0.319$  nm forms after 1500 turns, as shown in Fig. 3(b). The formation of this BCC-based phase after 1500 turns, which is likely due to the effect of lattice defects on the dynamic stability of phases [53–55], is in good agreement with earlier reports on the formation of BCC-based phases in SPD-processed Mg-based alloys [20,21,35–37], and is in line with the purpose of this study to synthesize a single-phase material with high atomic-scale elemental homogeneity.

To examine the thermal stability of the BCC-based phase, *in situ* XRD analyses were conducted using synchrotron radiation at different temperatures. The heating rate was 12 K/min and each pattern was taken in 20 s. As shown in Fig. 3(c), the BCC-based structure is incredibly stable up to 440 K suggesting the capability of the  $\text{Mg}_4\text{NiPd}$  phase for wide applications including hydrogen storage.

To examine the nanostructural features of the BCC-based phase, TEM observations were conducted. The BCC-based phase has a nanocrystalline morphology with an average grain size of  $10 \pm 4$  nm, as shown in the TEM bright-field (a) and dark-field (b) images in Fig. 4. The perfect ring pattern of the SAED analysis with several well-defined rings, taken from a region with a diameter of 300 nm, also confirms the presence of nano-sized polycrystals within the selected area. Examination of the TEM lattice images and the corresponding fast Fourier transform (FFT) diffractograms confirm that the BCC-based phase has a distorted structure and the atomic planes are not in an ideal geometrical condition (Fig. 4(c)), but some less-distorted structures can be partly detected (Fig. 4(d)).

### 3.2. Low hydrogen binding energy and room-temperature hydrogen storage

To examine the formation and stability of the BCC-based structure, the first-principles calculations were conducted. Fig. 5(a) shows the initial structure modeled by SQS and Fig. 5(b) shows the optimized structure. The examination of optimized lattice structure in Fig. 5(b) confirms that the BCC-based CsCl-type phase with a distorted lattice can remain stable provided that the three elements are well-mixed at the atomic scale over the two crystallographic BCC sites. The lattice parameter can be estimated from the optimized volume per atom as  $a=0.325$  nm (Fig. 5(b)). The ~2% overestimation from the experimental value of  $a=0.319$  nm is within reasonable accuracy of the GGA-PBE exchange-correlation function capabilities [56], and which suggests good correlation between the first-principles calculations and the

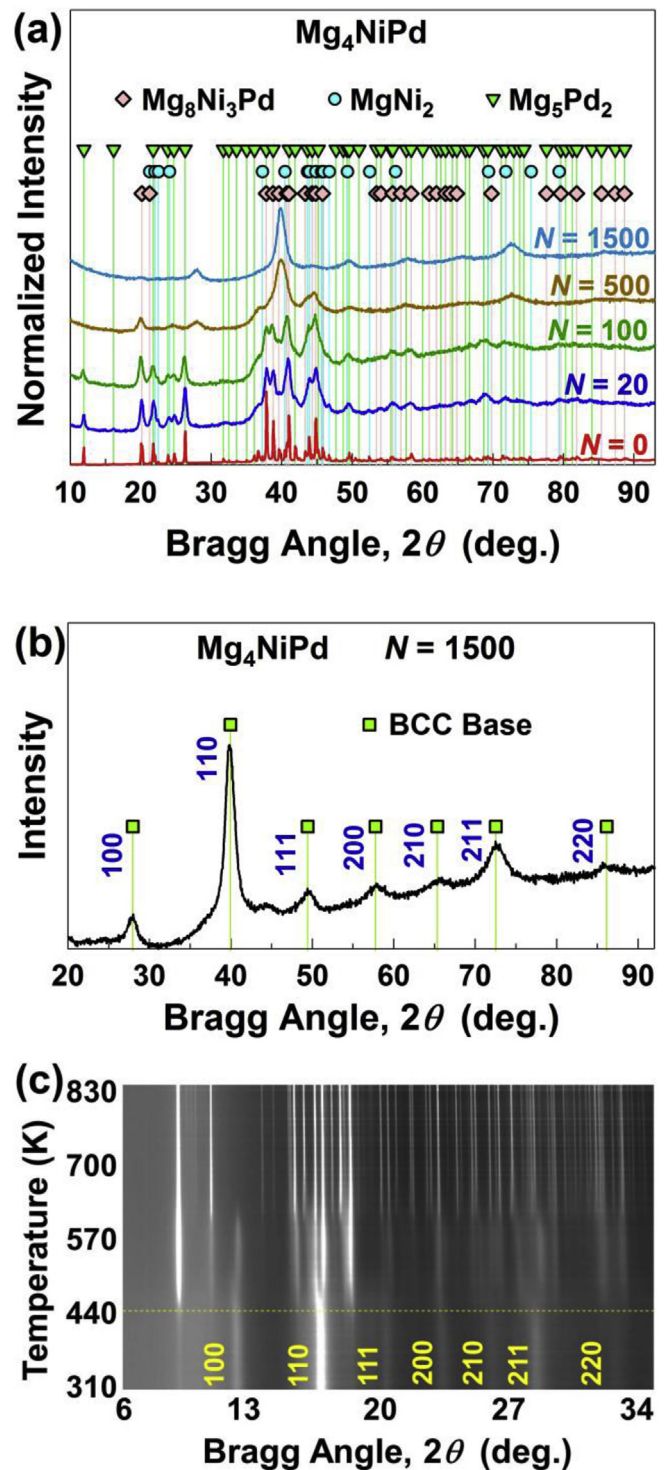
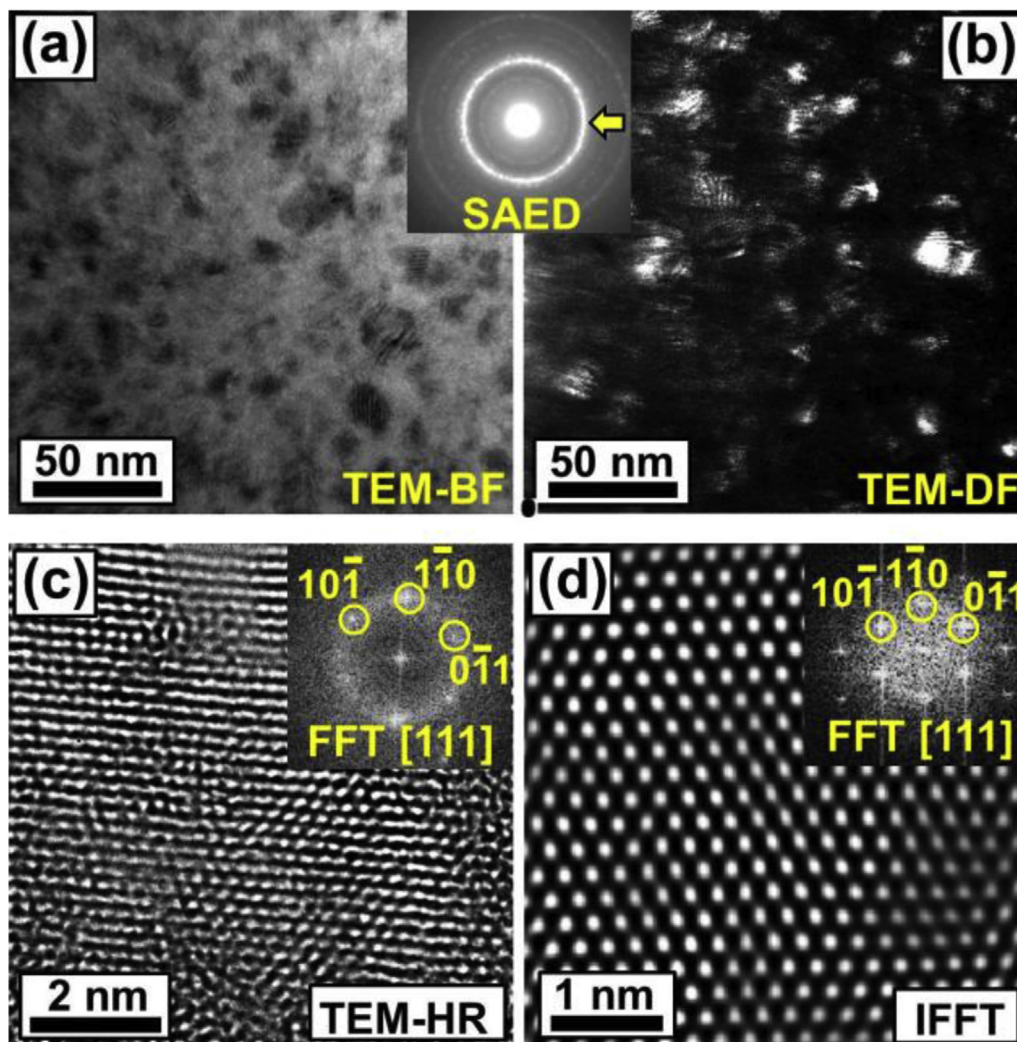


Fig. 3. A BCC-based CsCl-type structure with a lattice parameter of 0.319 nm is formed after 1500 HPT turns and remains thermally stable up to 440 K. XRD profiles obtained by (a, b)  $\text{Cu K}\alpha$  radiation and (c) *in situ* synchrotron radiation during heating under an argon atmosphere for the  $\text{Mg}_4\text{NiPd}$  processed by HPT for (a) 0–1500 turns and (b, c) 1500 turns. The numbers given in (b) and (c) indicate the atomic plane for the BCC-based structure; peak intensities in (c) correspond to the image brightness; the dotted line in (c) shows the decomposition temperature for the BCC-based structure.

experimental data. The plot of phonon density of states versus frequency, as shown in Fig. 5(c), shows that the BCC-based structure does not exhibit imaginary phonon frequencies, which implies that this phase is dynamically stable [50].



**Fig. 4.** The BCC-based structure has a distorted polycrystalline structure with an average grain size of  $10 \pm 4$  nm. TEM (a) bright-field image, (b) dark-field image and corresponding SAED pattern taken from an area with 300-nm diameter, (c) high-resolution image and corresponding FFT diffractogram and (d) the lattice image reconstructed by inverse FFT from the  $\{110\}$  diffractions for the  $\text{Mg}_4\text{NiPd}$  processed by HPT for 1500 turns. The dark-field image was obtained using the diffracted beams indicated by the arrow in the SAED pattern.

To examine the thermodynamics of the BCC-based structure for hydrogen storage, the hydrogen binding energies were calculated in three types of the most abundant octahedral sites, namely,  $4\text{Mg}-2\text{Ni}$ ,  $4\text{Mg}-1\text{Ni}-1\text{Pd}$  and  $4\text{Mg}-2\text{Pd}$ . Fig. 5(d) summarizes the theoretical hydrogen binding energies for the three main octahedral interstitial sites in the dynamically stable BCC-based structure. For the  $4\text{Mg}-2\text{Ni}$  sites, the hydrogen binding energy is negative, and thus, hydrogen may not be desorbed from these sites. For the  $4\text{Mg}-2\text{Pd}$  sites the hydrogen binding energy is positive and therefore hydrogen cannot occupy these sites. However, for the  $4\text{Mg}-1\text{Ni}-1\text{Pd}$  sites, with a composition that matches the  $\text{Mg}_4\text{NiPd}$  alloy, the hydrogen binding energy is close to the ideal binding energy for room-temperature hydrogen storage material (see Fig. 1). These calculations indicate that hydrogen can be absorbed and desorbed in certain octahedral sites in  $\text{Mg}_4\text{NiPd}$  at room temperature.

Fig. 6(a) shows the PCI results at room temperature (305 K) for the sample processed by HPT for 500 turns, after one and five hydrogenation/dehydrogenation cycles. The sample absorbed 0.6 wt% hydrogen with 0.5 wt% reversibility in the first cycle. However, the total absorption increases to 0.86 wt% (equivalent to  $\text{Mg}_4\text{NiPdH}_{2.25}$ ) after the fifth cycle, with an improved reversibility of 0.7 wt%. The current results on room temperature hydrogen storage introduce a

practical approach to designing and synthesizing new hydrogen storage materials that can reversibly store hydrogen at room temperature.

To examine the stability after cyclic hydrogenation and dehydrogenation, XRD analysis was performed after five PCI cycles. Fig. 6(b) shows the XRD profiles for the sample after the PCI measurements. It is apparent that the BCC-based phase remains stable after at least five hydrogenation/dehydrogenation cycles. There is no indication that trapped hydrogen was present. This confirms that the hydrogen is desorbed at room temperature, in good agreement with the PCI results shown in Fig. 6(a).

A question naturally arises now: where are the hydrogen atoms or what hydride was formed from the  $\text{Mg}_4\text{NiPd}$  alloy? In the context of this study, it was hard to identify the place of hydrogen or the structure of the hydride by *ex situ* analysis because of the room-temperature hydrogen storage reversibility and disappearance of the hydride phase during the *ex situ* analysis. To confirm that the hydrogen atoms were absorbed in the lattice, *in situ* XRD analysis under a hydrogen atmosphere at a pressure of 1.1 MPa (this pressure is not high enough for full hydrogenation, but it corresponds to the maximum experimentally achievable hydrogen pressure in our facility) was conducted. The results indicated a

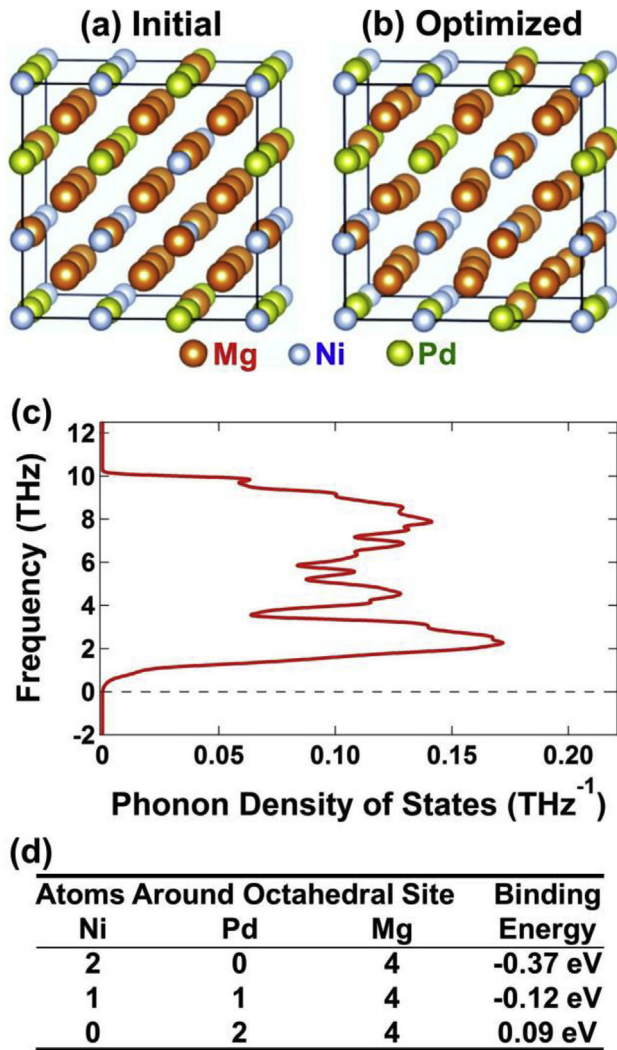


Fig. 5. The BCC-based structure is dynamically stable and shows low hydrogen binding energy at 4Mg-Ni-Pd octahedral sites. (a) Initial lattice structure, (b) optimized lattice structure, (c) phonon density of states curve and (d) calculated hydrogen binding energy at three main types of octahedral interstitial sites obtained from first-principles calculations for the Mg<sub>4</sub>NiPd with a BCC-based structure. Imaginary phonon frequencies are shown as negative values below the dotted line in (c); the hydrogen binding energies at the three different locations were averaged for each site type.

volume expansion of 1.03% after hydrogenation (see XRD peak shifts in Fig. 6(c)). This suggests that the hydrogen atoms started occupying the octahedral sites with low hydrogen binding energy at a pressure of 1.1 MPa, which naturally results in volume expansion.

#### 4. Conclusions

In summary, we report the design and fabrication of the Mg<sub>4</sub>NiPd alloy, having capacity to store hydrogen at room temperature due to its low hydrogen binding energy. The Mg<sub>4</sub>NiPd alloy with a BCC-based CsCl-type structure and a low hydrogen binding energy (a negative energy close to zero) was designed by employing first-principles calculations and synthesized by SPD using the HPT process with 1500 turns. This metastable alloy is highly homogeneous and is remarkably stable up to 440 K. It reversibly absorbs and desorbs 0.7 wt% hydrogen at room

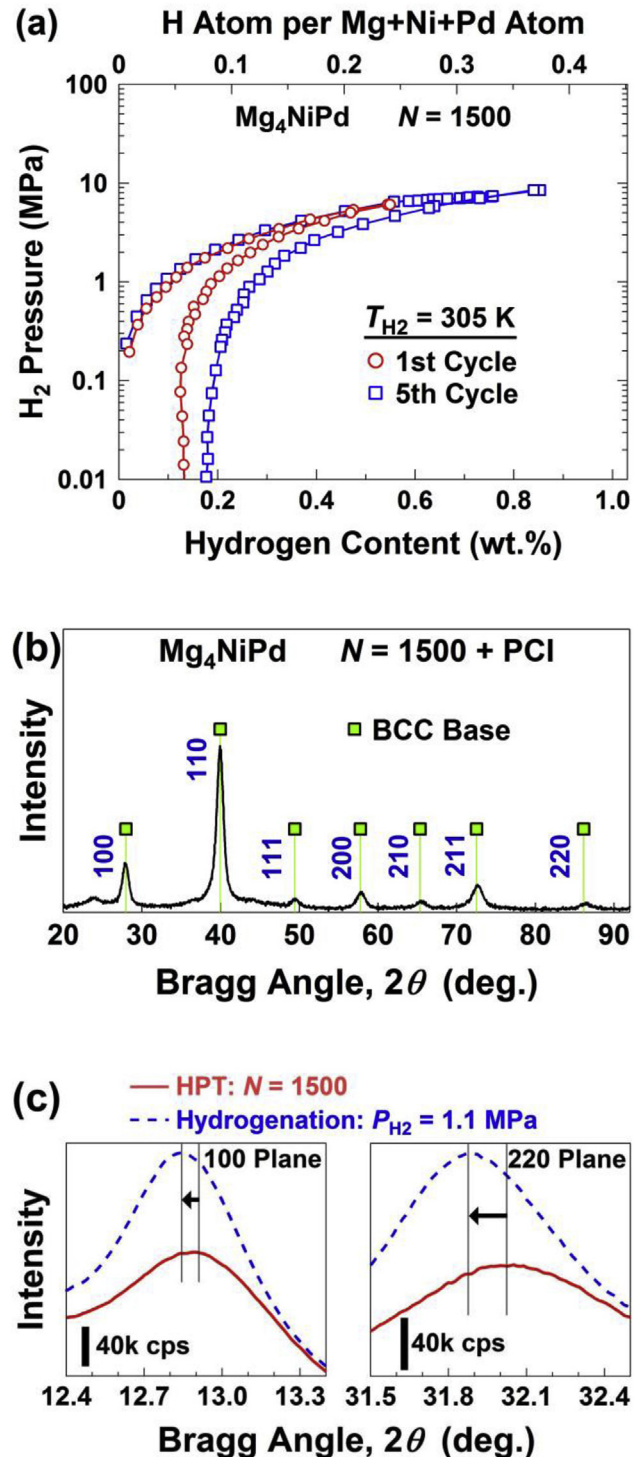


Fig. 6. The BCC-based Mg<sub>4</sub>NiPd phase shows room-temperature reversible hydrogen storage and remains stable after five hydrogenation/dehydrogenation cycles. (a) Hydrogen PCI results at 305 K under hydrogen pressures up to 10 MPa, (b) XRD profile after PCI measurements obtained using Cu Kα radiation, and (c) XRD profile obtained using *in situ* synchrotron radiation under a hydrogen atmosphere at a pressure of 1.1 MPa for the Mg<sub>4</sub>NiPd processed by HPT with 1500 turns. The vertical lines and arrows in (c) show the peak shifts due to hydrogenation.

temperature (305 K). To our knowledge, this is the first successful demonstration of tuning the dehydrogenation temperature of Mg-based alloys to room temperature by applying binding energy engineering principles. More importantly, it is worth emphasizing

that this strategy can be universally applied to design new materials with superior functional properties beyond the scope of the equilibrium phase diagrams.

## Acknowledgments

The authors acknowledge Mr. Fabien Cuvilly of Normandie Université, UNIROUEN, France for preparing the APT samples and ESRF for the beam-time allocation at SNBL, France. K.E. thanks MEXT, Japan, for a Grant-in-Aid for Scientific Research (B) (No. 16H04539). This study was supported in part by WPI-I2CNER, Japan, in part by gs2:Fonds De La Recherche Scientifique - FNRS, Belgium, and in part by a Grant-in-Aid for Scientific Research (S) from MEXT, Japan (No. 26220909). The HPT process was carried out in the International Research Center on Giant Straining for Advanced Materials (IRC-GSAM) at Kyushu University.

## References

- [1] A. Zuttel, A. Borgschulte, L. Schlapbach, *Hydrogen as a Future Energy Carrier*, Wiley VCH Press, Germany, 2008.
- [2] I.P. Jain, C. Lal, A. Lal, A. Jain, Hydrogen storage in Mg: a most promising material, *Int. J. Hydrogen Energy* 35 (2010) 5133–5144.
- [3] S. Orimo, Y. Nakamori, J.R. Eliseo, A. Zuttel, C.M. Jensen, Complex hydrides for hydrogen storage, *Chem. Rev.* 107 (2007) 4111–4132.
- [4] E. Wiberg, H. Goeltzer, R. Bauer, Synthesis of magnesium hydride from the elements, *Z. Naturforsch. B Chem. Sci.* 6 (1951) 394–395.
- [5] M. Dornheim, S. Doppiu, G. Barkhordarian, U. Boesenberg, T. Klassen, O. Gutfleisch, R. Bormann, Hydrogen storage in Mg-based hydrides and hydride composites, *Scripta Mater.* 56 (2007) 841–846.
- [6] K. Kadir, T. Sakai, I. Uehara, Synthesis and structure determination of a new series of hydrogen storage alloys;  $\text{RMg}_2\text{Ni}_9$  ( $R = \text{La, Ce, Pr, Nd, Sm}$  and  $\text{Gd}$ ) built from  $\text{MgNi}_2$  Laves-type layers alternating with  $\text{AB}_5$  layers, *J. Alloy. Comp.* 257 (1997) 115–121.
- [7] K. Kadir, T. Sakai, I. Uehara, Structural investigation and hydrogen capacity of  $\text{YMg}_2\text{Ni}_9$  and  $(\text{Y}_{0.5}\text{Ca}_{0.5})(\text{MgCa})\text{Ni}_9$ : new phases in the  $\text{AB}_2\text{C}_9$  system isostructural with  $\text{LaMg}_2\text{Ni}_9$ , *J. Alloy. Comp.* 287 (1999) 264–270.
- [8] T. Kohno, H. Yoshida, F. Kawashima, T. Inaba, I. Sakai, M. Yamamoto, M. Kanda, Hydrogen storage properties of new ternary system alloys:  $\text{La}_2\text{MgNi}_9$ ,  $\text{La}_5\text{Mg}_2\text{Ni}_{23}$ ,  $\text{La}_3\text{MgNi}_{14}$ , *J. Alloy. Comp.* 311 (2000) L5–L7.
- [9] N. Terashita, K. Kobayashi, T. Sasai, E. Akiba, Structural and hydriding properties of  $(\text{Mg}_{1-x}\text{Ca}_x)\text{Ni}_2$  Laves phase alloys, *J. Alloy. Comp.* 327 (2001) 275–280.
- [10] J.J. Reilly, R.H. Wiswall, Formation and properties of iron titanium hydride, *Inorg. Chem.* 13 (1974) 218–222.
- [11] J.H.N. Van Vucht, F.A. Kuijpers, H.C.A.M. Bruning, Reversible room-temperature absorption of large quantities of hydrogen by intermetallic compounds, *Philips Res. Rep.* 25 (1970) 133–140.
- [12] H. Emami, K. Edalati, A. Staykov, T. Hongo, H. Iwaoka, Z. Horita, E. Akiba, Solid-state reactions and hydrogen storage in magnesium mixed with various elements by high-pressure torsion: experiments and first-principles calculations, *RCS Adv* 6 (2016) 11665–11674.
- [13] H. Okamoto, M.E. Schlesinger, E.M. Mueller, *ASM Handbook Volume 3: Alloy Phase Diagrams*, ASM International, Materials Park, Ohio, 2016.
- [14] V.E. Kolesnichenko, V.V. Karonik, A.V. Ivanishev, Mg-Ni-Pd phase diagram in the magnesium rich region, *Izv. Akad. Nauk. SSSR, Metall* 4 (1981) 224–227.
- [15] K.P. Gupta, The Mg-Ni-Pd (magnesium-nickel-palladium) system, *J. Phase Equilibria Diffusion* 25 (2004) 191–194.
- [16] R.Z. Valiev, R.K. Islamgaliev, I.V. Alexandrov, Bulk nanostructured materials from severe plastic deformation, *Prog. Mater. Sci.* 45 (2000) 103–189.
- [17] R.Z. Valiev, Y. Estrin, Z. Horita, T.G. Langdon, M.J. Zehetbauer, Y.T. Zhu, Producing bulk ultrafine-grained materials by severe plastic deformation, *JOM (J. Occup. Med.)* 58 (4) (2006) 33–39.
- [18] A.P. Zhilyaev, T.G. Langdon, Using high-pressure torsion for metal processing: fundamentals and applications, *Prog. Mater. Sci.* 53 (2008) 893–979.
- [19] K. Edalati, Z. Horita, A review on high-pressure torsion (HPT) from 1935 to 1988, *Mater. Sci. Eng.* 652 (2016) 325–352.
- [20] K. Edalati, R. Uehiro, K. Fujiwara, Y. Ikeda, H.W. Li, X. Sauvage, R.Z. Valiev, E. Akiba, I. Tanaka, Z. Horita, Ultra-severe plastic deformation: evolution of microstructure, phase transformation and hardness in immiscible magnesium-based systems, *Mater. Sci. Eng.* 701 (2017) 158–166.
- [21] K. Edalati, H. Emami, Y. Ikeda, H. Iwaoka, I. Tanaka, E. Akiba, Z. Horita, New nanostructured phases with reversible hydrogen storage capability in immiscible magnesium-zirconium system produced by high-pressure torsion, *Acta Mater.* 108 (2016) 293–303.
- [22] K. Edalati, M. Matsuo, H. Emami, S. Itano, A. Alhamidi, A. Staykov, D.J. Smith, S. Orimo, E. Akiba, Z. Horita, Impact of severe plastic deformation on microstructure and hydrogen storage of titanium-iron-manganese intermetallics, *Scripta Mater.* 124 (2016) 108–111.
- [23] K. Edalati, H. Shao, H. Emami, H. Iwaoka, Z. Horita, E. Akiba, Activation of titanium-vanadium alloy for hydrogen storage by introduction of nanograins and edge dislocations using high-pressure torsion, *Int. J. Hydrogen Energy* 41 (2016) 8917–8924.
- [24] D.R. Leiva, A.M. Jorge, T.T. Ishikawa, J. Huot, D. Fruchart, S. Miraglia, C.S. Kiminami, W.J. Botta, Nanoscale grain refinement and H-sorption properties of  $\text{MgH}_2$  processed by high-pressure torsion and other mechanical routes, *Adv. Eng. Mater.* 12 (2010) 786–792.
- [25] K. Edalati, A. Yamamoto, Z. Horita, T. Ishihara, High-pressure torsion of pure magnesium: evolution of mechanical properties, microstructures and hydrogen storage capacity with equivalent strain, *Scripta Mater.* 64 (2011) 880–883.
- [26] T. Grosdidier, J.J. Fundenberger, J.X. Zou, Y.C. Pan, X.Q. Zeng, Nanostructured Mg based hydrogen storage bulk materials prepared by high pressure torsion consolidation of arc plasma evaporated ultrafine powders, *Int. J. Hydrogen Energy* 40 (2015) 16985–16991.
- [27] J.X. Zou, C.F. Perez-Brokate, R. Arruffat, B. Bolle, J.J. Fundenberger, X.Q. Zeng, T. Grosdidier, W.J. Ding, Nanostructured bulk Mg + MgO composite synthesized through arc plasma evaporation and high-pressure torsion for H-storage application, *Mater. Sci. Eng. B* 183 (2014) 1–5.
- [28] A. Revesz, Z. Kanya, T. Verebelyi, P.J. Szabo, A.P. Zhilyaev, T. Spassov, The effect of high-pressure torsion on the microstructure and hydrogen absorption kinetics of ball-milled  $\text{Mg}_{70}\text{Ni}_{30}$ , *J. Alloy. Comp.* 204 (2010) 83–88.
- [29] T. Hongo, K. Edalati, M. Arita, J. Matsuda, E. Akiba, Z. Horita, Significance of grain boundaries and stacking faults on hydrogen storage properties of  $\text{Mg}_2\text{Ni}$  intermetallics processed by high-pressure torsion, *Acta Mater.* 92 (2015) 46–54.
- [30] P. Thompson, D.E. Cox, J.B. Hastings, Rietveld refinement of Debye-Scherrer synchrotron X-ray data from  $\text{Al}_2\text{O}_3$ , *J. Appl. Crystallogr.* 20 (1987) 79–83.
- [31] J. Rodriguez-Carvajal, Recent advances in magnetic structure determination by neutron powder diffraction, *Physica B* 192 (1993) 55–69.
- [32] R. Pippan, S. Scheriau, A. Taylor, M. Hafok, A. Hohenwarter, A. Bachmaier, Saturation of fragmentation during severe plastic deformation, *Annu. Rev. Mater. Res.* 40 (2010) 319–343.
- [33] D.J. Lee, E.Y. Yoon, D.H. Ahn, B.H. Park, H.W. Park, L.J. Park, Y. Estrin, H.S. Kim, Dislocation density-based finite element analysis of large strain deformation behavior of copper under high-pressure torsion, *Acta Mater.* 76 (2014) 281–293.
- [34] M. Kawasaki, R.B. Figueiredo, Y. Huang, T.G. Langdon, Interpretation of hardness evolution in metals processed by high-pressure torsion, *J. Mater. Sci.* 49 (2014) 6586–6596.
- [35] H. Shao, K. Asano, H. Enoki, E. Akiba, Preparation and hydrogen storage properties of nanostructured Mg–Ni BCC alloys, *J. Alloy. Comp.* 477 (2009) 301–306.
- [36] X. Zhuang, Y. Zhang, Y. Zhu, Y. Qu, L. Zhan, N. Wan, H. Cheng, X. Guo, J. Chen, Z. Wang, L. Li, The effects of Pd and/or Zr additives on the structures and cyclic stabilities of  $\text{Mg}_{50}\text{Ni}_{50}$ -based electrode alloys, *Int. J. Hydrogen Energy* 40 (2015) 2768–2774.
- [37] K. Edalati, H. Emami, A. Staykov, D.J. Smith, E. Akiba, Z. Horita, Formation of metastable phases in magnesium-titanium system by high-pressure torsion and their hydrogen storage performance, *Acta Mater.* 99 (2015) 150–156.
- [38] A. Zunger, S.H. Wei, L.G. Ferreira, J.E. Bernard, Special quasirandom structures, *Phys. Rev. Lett.* 65 (1990) 353–356.
- [39] S. Kirkpatrick, C.D. Gelatt, M.P. Vecchi, Optimization by simulated annealing, *Science* 220 (1983) 671–680.
- [40] S. Kirkpatrick, Optimization by simulated annealing: quantitative studies, *J. Stat. Phys.* 34 (1984) 975–986.
- [41] A. Seko, K. Yuge, F. Oba, A. Kuwabara, I. Tanaka, T. Yamamoto, First-principles study of cation disordering in  $\text{MgAl}_2\text{O}_4$  spinel with cluster expansion and Monte Carlo simulation, *Phys. Rev. B* 73 (2006) 094116.
- [42] A. Seko, Y. Koyama, I. Tanaka, Cluster expansion method for multicomponent systems based on optimal selection of structures for density-functional theory calculations, *Phys. Rev. B* 80 (2009) 165122.
- [43] P.E. Blochl, Projector augmented-wave method, *Phys. Rev. B* 50 (1994) 17953–17979.
- [44] J.P. Perdew, K. Burke, M. Ernzerhof, Generalized gradient approximation made simple, *Phys. Rev. Lett.* 77 (1996) 3865–3868.
- [45] G. Kresse, *Ab initio* molecular dynamics for liquid metals, *J. Non-Cryst. Solids* 192 (1995) 222–229.
- [46] G. Kresse, J. Furthmuller, Efficiency of *ab-initio* total energy calculations for metals and semiconductors using a plane-wave basis set, *Comput. Mater. Sci.* 6 (1996) 15–50.
- [47] G. Kresse, D. Joubert, From ultrasoft pseudopotentials to the projector augmented-wave method, *Phys. Rev. B* 59 (1999) 1758–1775.
- [48] M. Methfessel, A.T. Paxton, High-precision sampling for Brillouin-zone integration in metals, *Phys. Rev. B* 40 (1989) 3616–3621.
- [49] K. Momma, F. Izumi, VESTA 3 for three-dimensional visualization of crystal volumetric and morphology data, *J. Appl. Crystallogr.* 44 (2011) 1272–1276.
- [50] A. Togo, I. Tanaka, First principles phonon calculations in materials science, *Scripta Mater.* 108 (2015) 1–5.

- [51] A.H. MacDonald, S.H. Vosko, P.T. Coleridge, Extensions of the tetrahedron method for evaluating spectral properties of solids, *J. Phys. C Solid State Phys.* 12 (1979) 2991–3002.
- [52] P.E. Blochl, O. Jepsen, O.K. Andersen, Improved tetrahedron method for Brillouin-zone integrations, *Phys. Rev. B* 49 (1994) 16223–16233.
- [53] B.B. Straumal, A.S. Gornakova, O.B. Fabrichnaya, M.J. Kiregel, A.A. Mazilkin, B. Baretzky, A.M. Gusak, S.V. Dobatkin, Effective temperature of high pressure torsion in Zr-Nb alloys, *High Temp. Mater. Process.* 31 (2012) 339–350.
- [54] V.L. Levitas, M. Javanbakht, Phase transformations in nanograin materials under high pressure and plastic shear: nanoscale mechanisms, *Nanoscale* 6 (2014) 162–166.
- [55] A. Badillo, P. Bellon, R.S. Averback, A phase field model for segregation and precipitation induced by irradiation in alloys, *Model. Simulat. Mater. Sci. Eng.* 23 (2015) 035008.
- [56] B. Grabowski, T. Hickel, J. Neugebauer, Ab initio study of the thermodynamic properties of nonmagnetic elementary fcc metals: exchange-correlation-related error bars and chemical trends, *Phys. Rev. B* 76 (2007) 24309.